Investigating the optimal size of anticancer nanomedicine

Li Tang[a], Xujuan Yang[b], Qian Yin[a], Kaimin Cai[a], Hua Wang[a], Isthier Chaudhury[a], Catherine Yao[a], Qin Zhou[c], Mincheol Kwon[a], James A. Hartman[b], Iwona T. Dobrucki[d], Lawrence W. Dobrucki[e], Luke B. Borst[f], Stéphane Lezmi[g], William G. Helferich[b,1], Andrew L. Ferguson[a,1], Timothy M. Fan[h,1], and Jianjun Cheng[a,e,1]

Departments of [a]Materials Science and Engineering, [b]Food Science and Human Nutrition, [e]Bioengineering, [g]Pathobiology, and [h]Veterinary Clinical Medicine, and [d]Beckman Institute for Advanced Science and Technology, University of Illinois at Urbana–Champaign, Urbana, IL, 61801; [c]Department of Pharmaceutical Science, Guangdong Pharmaceutical College, Guangzhou, Guangdong, 510006, China; and [f]Department of Population Health and Pathobiology, North Carolina State University, Raleigh, NC 27606

Edited* by Mark E. Davis, California Institute of Technology, Pasadena, CA, and approved September 15, 2014 (received for review June 19, 2014)

Nanomedicines (NMs) offer new solutions for cancer diagnosis and therapy. However, extension of progression-free interval and overall survival time achieved by Food and Drug Administration-approved NMs remain modest. To develop next generation NMs to achieve superior anticancer activities, it is crucial to investigate and understand the correlation between the physicochemical properties of NMs (particle size in particular) and their interactions with biological systems to establish criteria for NM optimization. Here, we systematically evaluated the size-dependent biological profiles of three monodisperse drug–silica nanoconjugates (NCs; 20, 50, and 200 nm) through both experiments and mathematical modeling and aimed to identify the optimal size for the most effective anticancer drug delivery. Among the three NCs investigated, the 50-nm NC shows the highest tumor tissue retention integrated over time, which is the collective outcome of deep tumor tissue penetration and efficient cancer cell internalization as well as slow tumor clearance, and thus, the highest efficacy against both primary and metastatic tumors in vivo.

nanomedicine | size effect | silica nanoparticle | mathematical model | drug delivery

O ver the last two to three decades, consensus has been reached that the size of anticancer nanomedicines (NMs) plays a pivotal role in determining their biodistribution, tumor penetration, cellular internalization, and clearance from blood plasma and tissues as well as excretion from body, and thus, it has significant impact on overall therapeutic efficacy against cancers (1–7). Although most clinically approved anticancer NMs have size ranging from 100 to 200 nm (8, 9), recent studies showed that anticancer NMs with smaller sizes exhibited enhanced performance in vivo, such as greater tissue penetration and enhanced tumor inhibition, particularly those with size around or smaller than 50 nm (5–7, 10–12). As such, there has been a major push recently in the field of anticancer NM to miniaturize nanoparticle (NP) size using novel chemistry and engineering design (13–17). One unanswered question, however, is whether additional miniaturization of NM size would be necessary and result in additional improved anticancer efficacy. Widely evaluated small molecular therapeutics (<1,500 Da and <2 nm) can traverse most tumor tissues freely (18). However, they diffuse away from tumor tissues rapidly and get cleared primarily into tumor blood capillaries, leading to minimal tumor accumulation (18). Macromolecules of relatively low molecular masses (<40,000 Da and <10 nm) were also shown to have low overall tumor retention because of both rapid permeation into and clearance from tumor tissues, behaving to some extent like small molecule drugs (18, 19). In conjunction with the renal clearance threshold (<10–15 nm) (20, 21) and interstitial/lymphatic fenestration (<20 nm) (22) for NPs, it becomes essential to carefully and comprehensively evaluate the in vivo behavior and anticancer efficacy of NMs in the size range of 20–50 nm to determine the optimal size of NM for cancer therapy.

In this study, we used monodisperse drug–silica nanoconjugates (NCs) that have identical physiochemical properties, except for

size, to investigate the size-dependent biodistribution and tumor tissue penetration and clearance as well as the overall efficacy. We focused on the NCs of 20 and 50 nm in this particularly interesting size range as well as the NC of 200 nm, the upper size limit of systemic NM to extravasate leaky tumor vasculature, which has a cutoff pore size larger than 200 nm for most tumors (23). Among these three representative sizes, the 50-nm NC showed the optimal balance of deep tissue penetration and high retention in tumors, which is in contrast with its larger counterpart (the 200-nm NC) of limited tumor tissue penetration and smaller counterpart (the 20-nm NC) of fast clearance from tumors, leading to overall low tumor retention for both. Therefore, 50 nm could be or could be close to the optimal size of NCs in the studied size range of 20–200 nm, ensuring not only the efficient distribution in, but also the protracted availability of drug-containing NC to the tumor tissues, resulting in superior anticancer efficacy against both primary and metastatic tumors.

Results and Discussion

To study the optimal size of NM for cancer therapy, we developed a precisely size-controlled NM, named drug–silica NC (24). Silica NP is an attractive platform for the development of NMs with excellently controlled sizes, high stability for biological evaluations, and complete clearance and good safety profiles for potential clinic applications (25–29). The designed drug–silica NCs had a hard silica core and a drug-conjugated silica outer layer with the surface coated with poly(ethylene glycol) (PEG) (Fig. 1A). The silica cores with precisely controlled

Significance

Understanding the interdependency of physiochemical properties of nanomedicine (NM) in correlation to its biological response and function is crucial for additional development of anticancer NM. Here, we prepared monodisperse drug–silica nanoconjugates in three distinct sizes (20, 50, and 200 nm) with other physiochemical properties controlled to be identical to investigate size-dependent biodistribution, tumor tissue penetration and clearance, and anticancer efficacy in various tumor models. We also developed a mathematical model of the spatiotemporal distribution of NM within a tumor to gain insight into the size-dependent interaction with tumor. Our studies show clear evidence that there is an optimal size of anticancer NM and that NM with the optimal size has the highest tumor retention integrated over time.

sizes were obtained by tuning the concentrations of tetraethyl orthosilicate, alcohol, water, and ammonia using the Stöber method (24). We conjugated camptothecin (Cpt), a cytotoxic quinoline alkaloid that inhibits the DNA enzyme topoisomerase I, to the size-controlled silica cores using a silanized derivative of Cpt (Fig. 1A), yielding the Cpt-NCs with the desired sizes of 200, 50, and 20 nm in diameter (Cpt-NC200, Cpt-NC50, and Cpt-NC20, respectively) (Fig. 1B). All three NCs had very narrow size distribution measured by scanning electron microscope (SEM) (Fig. 1B and Table 1) and dynamic light scattering (*SI Appendix, Fig. S1A*). The coefficient of variation values were less than 10%, indicating that the NCs were monodisperse by industrial standard (Table 1). These Cpt-NCs had similar drug loadings (15.9–16.6 wt%), release kinetics, surface PEG densities (0.22–0.24 PEG molecules/nm^2), ζ-potentials, and pharmacokinetics profiles in C57BL/6 mice ($t_{1/2}$ = 3.0–3.2 h) (Table 1 and *SI Appendix, Fig. S1*). Thus, the key physiochemical properties of these Cpt-NCs were identical, leaving NP size as the only variable to be studied for size impact on the interaction with biological systems.

With the highly controlled drug–silica NCs in hand, we first examined the impact of NC size on biodistribution and tumor tissue penetration as well as the outward clearance from tumors to identify the optimal size of NC for highest tumor retention. We first radiolabeled the 200-, 50-, and 20-nm silica NCs with copper-64 (^{64}Cu) cations (^{64}Cu-NC200, ^{64}Cu-NC50, and ^{64}Cu-NC20, respectively), administered them to athymic nude mice bearing s.c. human MCF-7 tumors through i.v. injection, and then, tracked their biodistribution with the PET imaging technique (Fig. 1C). Mice injected with ^{64}Cu-NC50 had the highest radioactivity in their tumor tissues among the three NCs tested 24 h postinjection (p.i.). This observation was confirmed by quantification of the absolute radioactivity in the harvested tumor tissues using a γ-counter, which showed that the ^{64}Cu-NC50–treated mice had 84.1% and 23.6% higher tumor accumulation than ^{64}Cu-NC200– and ^{64}Cu-NC20–treated mice, respectively (Fig. 1D and *SI Appendix, Fig. S2*). By comparing the accumulation ratio of tumor to muscle (Fig. 1E), we observed that smaller NCs (≤50 nm) could passively target tumor tissues more efficiently than larger NCs (200 nm), likely by the enhanced permeation and retention effect (18, 23). Importantly, ^{64}Cu-NC50 showed the highest passive tumor targeting effect among the three NCs in the MCF-7 human breast tumor model.
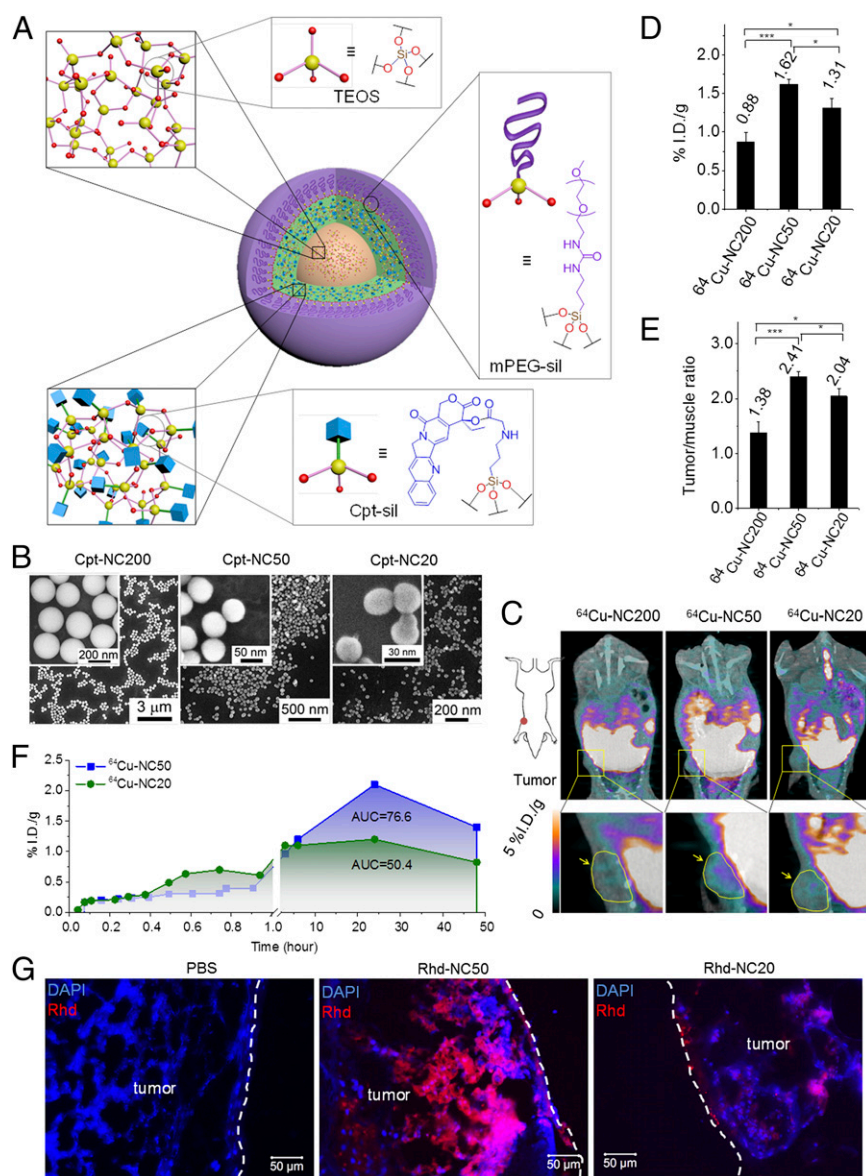

Fig. 1. Size-dependent biodistribution and tumor retention of drug–silica NCs. (A) Schematic illustration of the size-controlled drug–silica NCs. (B) SEM images of the Cpt-NCs. (C–E) In vivo biodistribution of ^{64}Cu-NCs of different sizes in athymic nude mice bearing s.c. MCF-7 human breast tumors. The athymic nude mice were injected i.v. with ^{64}Cu-NC200, ^{64}Cu-NC50, or ^{64}Cu-NC20 and then euthanized 24 h p.i. (n = 5). (C) Whole-body images were taken with a micro-PET/computed tomography imaging system. Yellow circles and arrows indicate the positions of tumors. (D) Mouse organs, including tumors, were collected and measured for radioactivity by γ-counter to determine the %I.D. per gram values. (E) The ratio of tumor to muscle was calculated based on the %I.D. per gram values of tumor and muscle of each mouse. All of the data are represented as the average ± SEM and analyzed by one-way ANOVA (Fisher; 0.01 < *P ≤ 0.05; **P ≤ 0.01; ***P ≤ 0.001). (F) Monitoring of the kinetics of tumor accumulation of ^{64}Cu-NC50 and ^{64}Cu-NC20 from 0 to 48 h p.i. The AUC was calculated by the trapezoidal rule up to 48 h. (G) Ex vivo tumor clearance study in MCF-7 tumors. MCF-7 tumors were ex vivo cultured with Rhd-NCs of different sizes in opti-MEM for 24 h to allow the silica NCs to penetrate into the tumors passively and then immersed in fresh opti-MEM to monitor the clearance of Rhd-NCs from the tumors. After another 48 h, the tumors were sectioned and imaged with a confocal fluorescence microscope. Representative images show the retention of Rhd-NCs (red) in tumor tissues. The nuclei were stained with 4′,6-diamidino-2-phenylindole (DAPI; blue). (Scale bar: 50 μm.)

Table 1. Characterization of the size controlled drug–silica NCs

Name of NC	D ± SD* (nm)	CV%[†]	PEG density[‡] (no./nm²)	Blood half-life (h)
Cpt-NC200	199.3 ± 14.8	7.4	0.237	3.23
Cpt-NC50	53.2 ± 4.9	9.2	0.239	3.04
Cpt-NC20	24.9 ± 2.3	9.2	0.222	3.12

*The sizes of NCs were measured by SEM. Average diameter (D) and standard deviation (SD) were calculated by measuring over 100 NCs in SEM images.

[†]Coefficient of variation (CV%) = SD/D.

[‡]The number of PEG molecules per nanometer² was calculated based on wt% of PEG per NC and its surface area.

We next focused on the 50- and 20-nm NCs to monitor their kinetics of accumulation in the MCF-7 tumors in live mice non-invasively over 48 h using dynamic PET (Fig. 1F). The radiation signal increased rapidly in the tumors of the mice receiving ^{64}Cu-NC20 during the first 3 h p.i., likely because of the fast tumor penetration of the 20-nm NC (24, 30). However, ^{64}Cu-NC50 started to show higher tumor accumulation than ^{64}Cu-NC20 at 6 h p.i. and persisted in tumors at higher levels until 48 h. The radiation signal within the tumor tissue of the ^{64}Cu-NC50–treated mice at 48 h p.i was 1.4% of injected dose per gram of tissue (I.D./g), which was 70% higher than that of ^{64}Cu-NC20–treated mice (0.82% I.D./g). The area under curve (AUC) of ^{64}Cu-NC50 was 1.52 times that of 20-nm NC over the 48-h period, suggesting that the 50-nm NC maintained overall higher concentration in tumors. The overall accumulation of the NCs in tumor depends on their extravasation and permeation rate in tumor tissues and the effectiveness of cellular internalization as well as the outward clearance from tumors. Both 50- and 20-nm NCs were internalized by MCF-7 cells, which was efficiently evidenced by an in vitro cell uptake experiment (*SI Appendix*, Fig. S3A). The passive tumor penetration depths of rhodamine (Rhd) -labeled 20-nm silica NC in MCF-7 tumor were 1.5- and 12.6-fold of that of Rhd-NC50 and Rhd-NC200, respectively, as determined in an ex vivo experiment (*SI Appendix*, Fig. S4), indicating that Rhd-NC20 could penetrate tumor tissues faster and deeper. In an in vivo experiment, mice bearing s.c. MCF-7 tumors were i.v.-injected with Rhd-NCs, and the tumors were collected 3 h p.i. for analyses. Indeed, more Rhd-NC20s were found in tumor tissues farther away from tumor blood vessels than Rhd-NC50 (*SI Appendix*, Fig. S5). These observations agree well with previous reports (5, 24, 30). However, such rapid permeation rate of 20-nm NC in the tumor interstitial space may lead to a lower degree of tumor accumulation, because the smallest NC (20 nm) can also be cleared faster from tumor tissues into blood or lymphatic vessels as well as surrounding tissues than larger NCs (19, 30). To compare the outward clearance rate, the harvested MCF-7 and 4T1 tumors with preaccumulated Rhd-NC50 or Rhd-NC20 in the tissues were immersed in fresh media to monitor the amount of cleared silica NCs in the media (*SI Appendix*, Fig. S6A). The results indicate that Rhd-NC20 was cleared at a higher rate than Rhd-NC50 over the 48-h period (*SI Appendix*, Fig. S6 B and C), resulting in less retention in the tumor tissues (Fig. 1G). Fast and deep tumor penetration could be the reason that 20-nm NC accumulated more in MCF-7 tumor tissues initially (first 3 h as shown in Fig. 1F). However, the 50-nm NC was retained in tumors for longer dwell times because of the relatively slower penetration into the tumor interstitial space, with a resultant overall enhanced accumulation in tumors over 48 h (Fig. 1 F and G). Therefore, 50 nm could be the optimal size of NM that balances the extravasation and permeation inside tumor tissues and the clearance from tumor to retain the highest concentrations within the immediate tumor and associated microenvironment.

To further develop insight into the size dependency of NM in tumor accumulation and retention, we developed a mathematical model of the spatiotemporal distribution of NPs within a spherically symmetric tumor. We modeled NP diffusion in and out of the tumor spheroid, cell surface association and dissociation, and cellular internalization and externalization. Model parameters were fitted to experimental data of our silica NCs of 200, 50, and 20 nm in diameter (24), and best fit linear regression models were used to interpolate to NP sizes within this range (31–34). Full details of our model, parameter fitting, and numerical solution techniques are provided in *SI Appendix*. We solved our model for the spatiotemporal mass concentration of internalized NPs within a spherical tumor with a radius of 3.5 mm over a time horizon of 48 h. In Fig. 2 A–C, we illustrate the predictions of our model for NPs of diameters 200, 50, and 20 nm. The precise structure of the spatiotemporal concentration field results from the complex interplay of the NP diffusive transport and cellular uptake kinetics. The radial penetration of the NPs into the tumor spheroid is dictated in large part by the NP mobility, with the reduced diffusivity of the larger NPs resulting in a shallower depth of penetration. The temporal evolution of the profile is driven by the decay kinetics of the NPs in the bulk, but it is also controlled by the transport, surface association, and internalization of the NPs into cancer cells. The AUC of the concentration of internalized NPs within the tumor is an important parameter to compare the NP drug delivery effectiveness. In Fig. 2D, we present the model predictions of AUCs for 200, 50, and 20 nm NPs ($AUC_{50 nm} > AUC_{20 nm} > AUC_{200 nm}$), which are in excellent agreement with the experimental results (Fig. 1 D–F). The result suggests that the diffusivity and cellular uptake kinetics of the 50-nm NPs give rise to elevated dwell time within tumor tissue relative to the 20- and 200-nm NPs.

To verify the optimal size identified by both experiment and mathematical modeling, we next investigated whether the enhanced tumor retention of 50-nm NM could directly impart
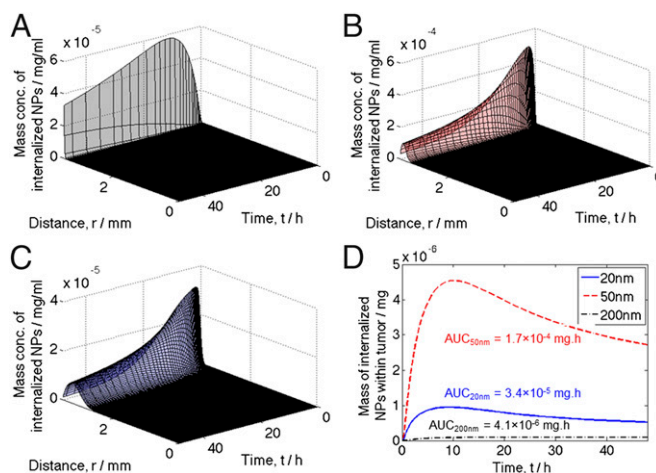
Fig. 2. Spatiotemporal modeling of size-dependent NP accumulation and retention in tumors. (A–C) Predicted concentration fields for the mass of internalized NPs within a spherically symmetric tumor as a function of radial distance from the tumor center (r) and time (t) for NPs of diameters of (A) 200, (B) 50, and (C) 20 nm. Full details of the model specification, parameterization, and solution are provided in *SI Appendix*. (D) Model predictions of the mass of internalized NPs as a function of time for the three sizes of NPs over a 48-h time horizon. The ordinate of the plot records the mass of internalized NPs within the spherical tumor, corresponding to the spatial integral $\int_0^R 4\pi r^2 dr M_i(t,r)$, where $R = 3.5$ mm is the tumor radius, and $M_i(t,r)$ is the spatiotemporal mass concentration of internalized NPs within the tumor. The AUC corresponds to the double integral $\int_0^T dt \int_0^R 4\pi r^2 dr M_i(t,r)$, where $t = 48$ h, and it represents a proxy measure of NP effectiveness in accumulating within the tumor. Both integrals are evaluated by numerical quadrature.

amplified therapeutic efficacy in treating s.c.-implanted MCF-7 human breast tumors in athymic nude mice. MCF-7 is an estrogen-dependent, noninvasive human breast cancer cell line that is extensively studied as a xenograft model for ER$^+$/HER2$^-$ breast cancer (35). In an acute antitumor efficacy study, the mice bearing MCF-7 tumors (initial tumor size was 49.3 mm^3 on day 0) were treated i.v. with Cpt-NC200, Cpt-NC50, and Cpt-NC20 of 20 mg Cpt equivalent/kg three times on days 0, 4, and 8, and PBS was used as a sham negative control group (*SI Appendix*, Fig. S7 *A* and *B*). All mice were euthanized on day 12. The average tumor weight increased 23.5% in the PBS control group over 12 d (*SI Appendix*, Fig. S7 *C* and *D*). As expected, Cpt-NC200 showed very limited effect on tumor growth inhibition, and the average tumor weight on day 12 remained nearly the same as the original because of low tumor accumulation. Both Cpt-NC50 and Cpt-NC20 were substantially more efficacious than Cpt-NC200 and resulted in ~50% tumor weight reduction (*SI Appendix*, Fig. S7*D*). The tumors from all groups were excised, sectioned, and stained for Ki67 and terminal deoxynucleotidyl transferase-mediated deoxyuridine triphosphate nick end (TUNEL) to determine the proliferation index and apoptosis index. The treatment with Cpt-NCs ≤ 50 nm resulted in a significantly reduced proliferation index and an increased apoptosis index compared with Cpt-NC200 and Cpt-NC20 (Fig. 3 *A–D*). Cpt-NC50 reduced the proliferation index to 42.8 ± 2.6%, which was significantly lower than both Cpt-NC200 (68.6 ± 0.9%) and Cpt-NC20 (50.5 ± 1.8%) (Fig. 3 *A* and *C*). Cpt-NC50 also triggered a significantly higher apoptosis index (21.0 ± 1.8%) than Cpt-NC200 (7.2 ± 0.3%) or Cpt-NC20 (15.3 ± 1.2%) (Fig. 3 *B* and *D*). Together, Cpt-NC50 showed the highest efficacy against MCF-7 tumors with an apoptosis-to-proliferation index ratio of 61.4 ± 4.8%, which was 6.0- and 2.1-fold higher than those of Cpt-NC200 (10.2 ± 0.5%) and Cpt-NC20 (28.6 ± 2.2%) (Fig. 3*E*).

To evaluate the tumor growth inhibition effect by Cpt-NCs of various sizes over a longer period, a separate efficacy study was designed similarly, except for adding blank silica NP (negative control) and irinotecan (positive control) as the control groups (*SI Appendix*, Fig. S8 *A* and *B*). Irinotecan was administered i.p. at 100 mg/kg, which was dosed five times higher than Cpt-NCs (20 mg/kg) (36). Compared with the PBS and the blank NP negative control groups, all other treatment groups showed superior growth inhibition of the MCF-7 tumor (Fig. 3*F* and *SI Appendix*, Fig. S8*C*). Mice that received Cpt-NCs or irinotecan also showed improved survival probability and increased median duration of time to end point (Fig. 3 *G* and *H*). Cpt-NC50 and Cpt-NC20 improved survival times by 76.5% and 61.8%, respectively, with significantly longer time to end point than that of Cpt-NC200. Importantly, among the Cpt-NCs of three different sizes, Cpt-NC50 was the most efficacious in terms of tumor growth inhibition and survival improvement. Interestingly, Cpt-NC50 showed significantly higher efficacy compared with Cpt-NC200 starting as early as day 6 (*SI Appendix*, Fig. S8*C*), whereas the statistical significance between Cpt-NC20 and Cpt-NC200 appeared after 18 d of experimentation. Treatment with Cpt-NC50 resulted in markedly smaller mean tumor burden (107 ± 13 mm^3) at day 40 compared with Cpt-NC200 (261 ± 46 mm^3) and Cpt-NC20 (228 ± 42 mm^3) (Fig. 3*F*), providing definitive evidence that Cpt-NC50 is the most effective in reducing tumor burden among all three NCs tested. There was no statistically significant difference for tumor sizes or survival rates between the Cpt-NC50 and the irinotecan groups. No significant changes of body weight and food intake were observed for the mice in all of the Cpt-NC groups (*SI Appendix*, Fig. S9). However, treatment with irinotecan produced higher toxicity in mice, which was evidenced by the notable body weight drop during the course of the study (*SI Appendix*, Fig. S9*A*). Thus, Cpt-NC50 was able to exert comparable anticancer activities as free irinotecan with
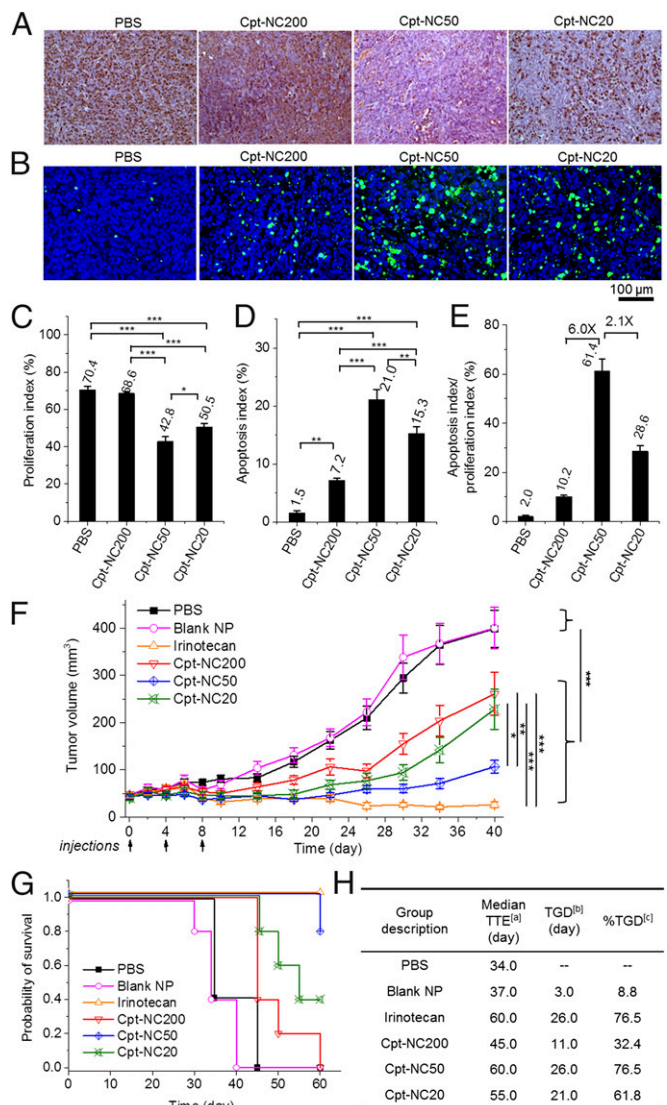

Fig. 3. Size-dependent antitumor efficacy in a primary tumor model. (*A–E*) In an acute efficacy study, athymic nude mice bearing MCF-7 human breast tumors were treated three times (every 4 d) by i.v. injection of PBS (1×), Cpt-NC200 (20 mg Cpt/kg), Cpt-NC50 (20 mg Cpt/kg), or Cpt-NC20 (20 mg Cpt/kg) on days 0, 4, and 8. (*A* and *C*) The collected MCF-7 tumors (*n* = 20) were sectioned and further stained with Ki67 to analyze the proliferation index of the tumor tissues. (*A*) Representative images and (*C*) quantification of Ki67 stains are shown. (*B* and *D*) The MCF-7 tumors (*n* = 20) were also stained with TUNEL (green) and DAPI (blue) for apoptosis analyses of the tumor tissues. (*B*) Representative images and (*D*) quantification by ImageJ of TUNEL stains are shown. (Scale bar: *A* and *B*, 100 μm.) (*E*) The ratio of apoptosis index to proliferation index indicates the overall efficacy of the Cpt-NCs. (*F–H*) In a long-term efficacy study, athymic nude mice bearing MCF-7 tumors were treated three times (every 4 d) by i.v. injection of PBS (1×), blank silica NPs, Cpt-NC200 (20 mg Cpt/kg), Cpt-NC50 (20 mg Cpt/kg), or Cpt-NC20 (20 mg Cpt/kg) on days 0, 4, and 8. Irinotecan (100 mg/kg) was administrated i.p. on days 0, 7, and 14. (*F*) Average tumor sizes of each group were monitored over the course of the study (*n* = 20). (*G*) Kaplan–Meier plots for all groups are shown. Loss of mice was because of treatment-related death, nontreatment-related death, or euthanasia after the end point (400 mg) had been reached (*n* = 5). (*H*) Survival analysis of the athymic nude mice bearing MCF-7 tumors. Each mouse was euthanized when the tumor size reached the end point or on day 60. [a]Time (days) to end point (TTE). [b]Treated group (T) − PBS group (C) = difference between TTE (days) of T vs. C (TGD). [c](T − C)/C (%TGD). All of the data are represented as average ± SEM and analyzed by one-way ANOVA (Fisher; 0.01 < *P* ≤ 0.05; **P ≤ 0.01; ***P ≤ 0.001).

substantially reduced toxicity. With respect to NC size effects, Cpt-NC50 was much more efficacious than Cpt-NC200 and Cpt-NC20 against an s.c.-implanted xenograft primary tumor.

Metastatic cancer is regarded as an incurable disease by conventional methods, including surgical resection, chemotherapy, and radiation therapy, and responsible for over 90% of cancer-related death (37). NM may offer new solutions for improving the prevention or treatment of tumor metastases. Despite extensive studies on NMs for the treatment of primary tumors, very few investigations have explored the efficacy of NMs against tumor metastases, and there are no studies that characterize the size effect of NMs on the efficacy against metastatic cancer. After we showed that Cpt-NC50 was the most efficacious in a breast primary tumor model, we went on to evaluate the size-dependent efficacy of Cpt-NCs in inhibiting the 4T1 murine breast cancer metastasis to lung tissues; 4T1 tumor is highly tumorigenic and invasive and can spontaneously metastasize to distant sites, such as the lung parenchyma (38), and 4T1 cells, which were luciferase-engineered for noninvasive monitoring of tumor growth in live animals using the bioluminescence (BL) imaging technique, were injected i.v. into BALB/c mice on day 0 to establish an experimental metastatic tumor model (39). The mice were treated with different Cpt-NCs as well as irinotecan starting from day 1 to examine the efficacy of metastasis inhibition (*SI Appendix*, Fig. S10). The BL imaging of the control mice (PBS group) on days 8 and 12 confirmed the existence of metastatic 4T1 tumors proliferating within lung parenchyma (Fig. 4*A*). As shown in Fig. 4 *A* and *C*, 12 d post-tumor inoculation, the BL signal emitted from the lung tissues of mice treated with PBS, Cpt-NC200, or Cpt-NC20 intensified rapidly and progressively. There were essentially no difference in BL intensities among the Cpt-NC200 and Cpt-NC20 groups and the PBS group, suggesting very limited efficacy of these two NCs for metastasis inhibition. However, the BL signal was markedly lower in the mice treated with Cpt-NC50 and irinotecan and increased at a much slower rate, suggesting that Cpt-NC50 exerted greater anticancer activities compared with Cpt-NC20 and Cpt-NC200, achieving comparable effects as free irinotecan (Fig. 4 *A* and *C*).

To further analyze lung pathology both macroscopically and microscopically, lung tissues were harvested from inoculated mice for detailed gross and histopathological evaluation. Tumor nodules on the surface of the lungs were counted manually with the aid of dissecting microscopy (Fig. 4 *B* and *D*). The results indicated that the treatment of Cpt-NC50 significantly reduced the number of macroscopic tumor nodules (77.3 ± 9.3 per lung) compared with the PBS group (108.8 ± 9.8 per lung) (Fig. 4*D*), which was consistent with the BL signal analysis (Fig. 4*C*). We also scaled the metastatic lungs based on the percentage of lung surface covered by tumor nodules (*SI Appendix*, Fig. S11*B*). The Cpt-NC50 group had an average score (3.0 ± 0.4) that was comparable with that of the irinotecan group (2.9 ± 0.2) and much lower than those of the Cpt-NC200 (3.7 ± 0.4) and Cpt-NC20 (3.8 ± 0.2) groups (*SI Appendix*, Fig. S11*A*). The results were further confirmed by sectioning the lungs and performing the histopathological analysis. Correlating with gross evaluation, there was a prominent reduction in the number of microscopic tumor nodules observed in the lung sections collected from the mice treated with Cpt-NC50 (Fig. 4*E*). Tumor metastases were not observed in other organs during the course of the study (*SI Appendix*, Fig. S12). Collectively, Cpt-NC50 outperformed Cpt-NC200 and Cpt-NC20 with respect to inhibiting the progression of 4T1 cell metastasis to lung tissues, and Cpt-NC50 showed comparable anticancer activity with that of irinotecan. In addition, the treatment of Cpt-NC50 did not cause any significant change of body weight, food intake, or histological damage to other tissues during the course of the study (*SI Appendix*, Figs.
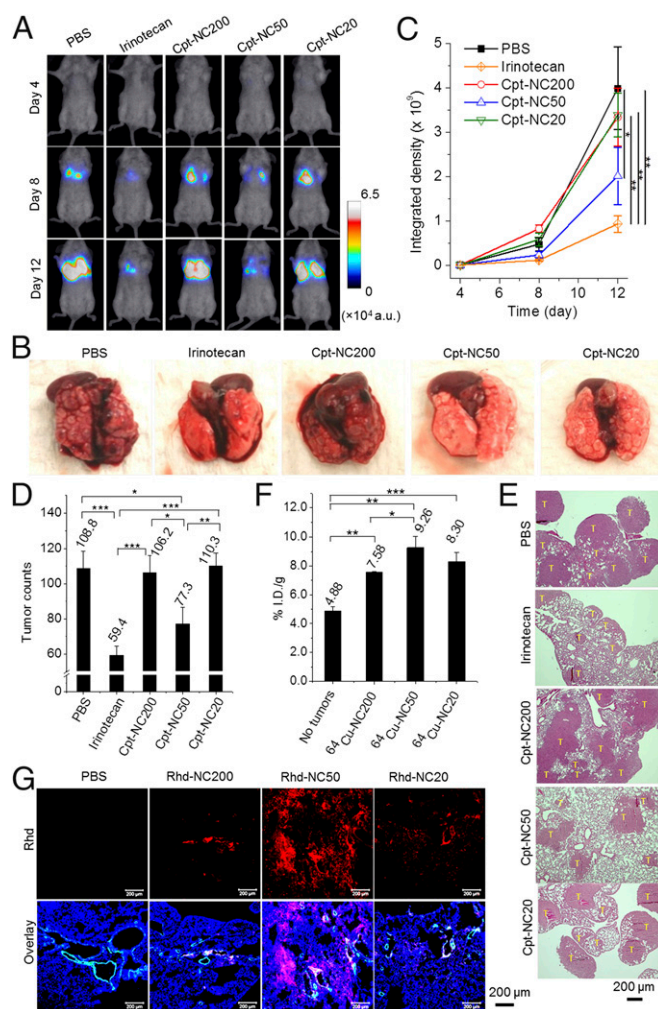

Fig. 4. Size-dependent antitumor efficacy in a metastatic tumor model. (*A–E*) 4T1 metastatic lung tumors were induced in mice by i.v. injection of luciferase-engineered murine 4T1 breast cancer cells into BALB/c mice on day 0. The mice were treated with i.v. injection of PBS (1×), Cpt-NC200 (20 mg Cpt/kg), Cpt-NC50 (20 mg Cpt/kg), or Cpt-NC20 (20 mg Cpt/kg) and i.p. injection of irinotecan (20 mg/kg) on days 1, 5, and 9 (n = 9–12). Representative (*A*) BL images and (*B*) lung pictures at necropsy are shown for each treatment group on day 12. (*C*) BL signals were analyzed to semiquantify 4T1 cell metastasis progression using ImageJ. Photon emission is represented as integrated density, and the measuring threshold is empirically set as 5,000. (*D*) Lungs were excised at necropsy and fixed in 10% (vol/vol) formalin. Tumor nodules on the lungs were counted and averaged. (*E*) Fixed lung tissues were embedded in paraffin, sectioned into 5-μm thickness, and then, stained with H&E. Sectioned tissues were observed under a microscope at 50× magnification. Representative images of the lung tissues are shown. T: tumor tissue. (Scale bar: 200 μm.) (*F*) In vivo biodistribution study in BALB/c mice bearing 4T1 metastatic tumors in lungs (n = 5). BALB/c mice with 4T1 metastatic tumors in lungs were injected i.v. with ^{64}Cu-NC200, ^{64}Cu-NC50, or ^{64}Cu-NC20 to investigate the biodistribution. Mice were euthanized 24 h p.i. (*G*) In vivo tumor penetration study in BALB/c mice bearing 4T1 metastatic tumors in lungs (n = 3). BALB/c mice with 4T1 metastatic tumors in lungs were injected i.v. with Rhd-NC200, Rhd-NC50, or Rhd-NC20. Mice were euthanized 24 h p.i. The lungs were sectioned in optimum cutting temperature compound and stained with CD31 to indicate the blood vessels (green). Representative images show the distribution of Rhd-NCs (red) in the lung tissues with metastatic 4T1 tumors. The nuclei were stained with DAPI (blue). All of the data are represented as average ± SEM and analyzed by one-way ANOVA (Fisher; 0.01 < *P ≤ 0.05; **P ≤ 0.01; ***P ≤ 0.001).

S12 and S13), indicating that acute toxicity associated with Cpt-NC50 in mice is clinically negligible. Similarly, as observed in

primary MCF-7 tumors, the accumulation of ^{64}Cu-NC50 in lungs with metastatic 4T1 tumors was 22.3% and 11.7% higher than ^{64}Cu-NC200 and ^{64}Cu-NC20, respectively (Fig. 4*F* and *SI Appendix*, Fig. S14). Interestingly, the accumulation of the NCs of all sizes in lungs with metastatic tumors was significantly higher than that in lungs without tumors, probably because of tumor vascularity and cancer cell internalization (Fig. 4*F*). In addition, Rhd-NC50 also showed increased retention in the lung tissues with metastatic 4T1 tumors, which was evidenced by the tissue section analyses compared with Rhd-NC20 and Rhd-NC200 (Fig. 4*G*). The enhanced tumor accumulation of 50-nm NCs in both primary and metastatic tumors likely contributes to the improved anticancer efficacy observed in both tumor models.

In conclusion, our investigation using monodisperse drug–silica NCs with discrete sizes provides clear theoretical and experimental evidence that the size of NM plays a vital role in determining its biological property and antitumor activity. The 50-nm drug–silica NC outperforms its smaller (20 nm) and larger (200 nm) analogs in overall tumor tissue accumulation and retention, and thus, shows the highest efficacy against both primary and metastatic tumors. Therefore, 50 nm could be or could be close to the optimal size of the PEG-coated anticancer drug–silica NC that balances extravasation, inward permeation inside tumor tissues, tumor cell internalization, and outward diffusion and clearance from tumor to retain the highest effective drug concentrations in tumors. Many surface PEGylated anticancer NMs are in various stages of preclinical or clinical development. Because the size and the surface property of an NM likely dictate its overall biological property, PEG-coated NMs may share many similarities with respect to their size dependency of biological activities. Our study and confirmation of the existence of the optimal size of the PEG-coated drug–silica NC clearly show the importance of controlling the size and dispersion of PEGylated NMs and the potential of further improving their antitumor efficacy by identifying the optimal size against a specific cancer. However, whether the optimal size of other PEGylated NMs remains at or around 50 nm requires further study.

Materials and Methods

Cpt-NCs with controlled sizes were prepared as previously reported (24) and used for all efficacy studies. Details describing preparation and characterization of size-controlled silica NCs; size-dependent biodistribution, tumor penetration and clearance, and cellular internalization studies; size-dependent efficacy studies in a primary tumor model; size-dependent efficacy studies in a metastatic tumor model; and spatiotemporal modeling of NP uptake into tumors can be found in *SI Appendix*.

1. Peer D, et al. (2007) Nanocarriers as an emerging platform for cancer therapy. *Nat Nanotechnol* 2(12):751–760.
2. Davis ME, Chen ZG, Shin DM (2008) Nanoparticle therapeutics: An emerging treatment modality for cancer. *Nat Rev Drug Discov* 7(9):771–782.
3. Jain RK, Stylianopoulos T (2010) Delivering nanomedicine to solid tumors. *Nat Rev Clin Oncol* 7(11):653–664.
4. Petros RA, DeSimone JM (2010) Strategies in the design of nanoparticles for therapeutic applications. *Nat Rev Drug Discov* 9(8):615–627.
5. Cabral H, et al. (2011) Accumulation of sub-100 nm polymeric micelles in poorly permeable tumours depends on size. *Nat Nanotechnol* 6(12):815–823.
6. Jiang W, Kim BYS, Rutka JT, Chan WCW (2008) Nanoparticle-mediated cellular response is size-dependent. *Nat Nanotechnol* 3(3):145–150.
7. Reddy ST, et al. (2007) Exploiting lymphatic transport and complement activation in nanoparticle vaccines. *Nat Biotechnol* 25(10):1159–1164.
8. Uster PS, Working PK, Vaage J (1998) Pegylated liposomal doxorubicin (DOXIL®, CAELYX®) distribution in tumour models observed with confocal laser scanning microscopy. *Int J Pharm* 162(1-2):77–86.
9. Gradishar WJ, et al. (2005) Phase III trial of nanoparticle albumin-bound paclitaxel compared with polyethylated castor oil-based paclitaxel in women with breast cancer. *J Clin Oncol* 23(31):7794–7803.
10. Wang H, et al. (2009) A supramolecular approach for preparation of size-controlled nanoparticles. *Angew Chem Int Ed Engl* 48(24):4344–4348.
11. Goodman TT, Olive PL, Pun SH (2007) Increased nanoparticle penetration in collagenase-treated multicellular spheroids. *Int J Nanomedicine* 2(2):265–274.
12. Tang L, et al. (2012) Aptamer-functionalized, ultra-small, monodisperse silica nanoconjugates for targeted dual-modal imaging of lymph nodes with metastatic tumors. *Angew Chem Int Ed Engl* 51(51):12721–12726.
13. Salem AK, Searson PC, Leong KW (2003) Multifunctional nanorods for gene delivery. *Nat Mater* 2(10):668–671.
14. Mitragotri S, Lahann J (2009) Physical approaches to biomaterial design. *Nat Mater* 8(1):15–23.
15. Nel AE, et al. (2009) Understanding biophysicochemical interactions at the nano-bio interface. *Nat Mater* 8(7):543–557.
16. Yu T, Malugin A, Ghandehari H (2011) Impact of silica nanoparticle design on cellular toxicity and hemolytic activity. *ACS Nano* 5(7):5717–5728.
17. Farokhzad OC, et al. (2006) Targeted nanoparticle-aptamer bioconjugates for cancer chemotherapy in vivo. *Proc Natl Acad Sci USA* 103(16):6315–6320.
18. Matsumura Y, Maeda H (1986) A new concept for macromolecular therapeutics in cancer chemotherapy: Mechanism of tumoritropic accumulation of proteins and the antitumor agent smancs. *Cancer Res* 46(12):6387–6392.
19. Dreher MR, et al. (2006) Tumor vascular permeability, accumulation, and penetration of macromolecular drug carriers. *J Natl Cancer Inst* 98(5):335–344.
20. Choi CHJ, Zuckerman JE, Webster P, Davis ME (2011) Targeting kidney mesangium by nanoparticles of defined size. *Proc Natl Acad Sci USA* 108(16):6656–6661.
21. Shilo M, Reuveni T, Motiei M, Popovtzer R (2012) Nanoparticles as computed tomography contrast agents: Current status and future perspectives. *Nanomedicine (Lond)* 7(2):257–269.
22. Moghimi SM, Hunter AC, Murray JC (2005) Nanomedicine: Current status and future prospects. *FASEB J* 19(3):311–330.
23. Hobbs SK, et al. (1998) Regulation of transport pathways in tumor vessels: Role of tumor type and microenvironment. *Proc Natl Acad Sci USA* 95(8):4607–4612.
24. Tang L, Fan TM, Borst LB, Cheng J (2012) Synthesis and biological response of size-specific, monodisperse drug-silica nanoconjugates. *ACS Nano* 6(5):3954–3966.
25. Ashley CE, et al. (2011) The targeted delivery of multicomponent cargos to cancer cells by nanoporous particle-supported lipid bilayers. *Nat Mater* 10(5):389–397.
26. Della Rocca J, Huxford RC, Comstock-Duggan E, Lin W (2011) Polysilsesquioxane nanoparticles for targeted platin-based cancer chemotherapy by triggered release. *Angew Chem Int Ed Engl* 50(44):10330–10334.
27. Benezra M, et al. (2011) Multimodal silica nanoparticles are effective cancer-targeted probes in a model of human melanoma. *J Clin Invest* 121(7):2768–2780.
28. Meng H, et al. (2011) Aspect ratio determines the quantity of mesoporous silica nanoparticle uptake by a small GTPase-dependent macropinocytosis mechanism. *ACS Nano* 5(6):4434–4447.
29. Tang L, Cheng J (2013) Nonporous silica nanoparticles for nanomedicine application. *Nano Today* 8(3):290–312.
30. Perrault SD, Walkey C, Jennings T, Fischer HC, Chan WCW (2009) Mediating tumor targeting efficiency of nanoparticles through design. *Nano Lett* 9(5):1909–1915.
31. van Osdol W, Fujimori K, Weinstein JN (1991) An analysis of monoclonal antibody distribution in microscopic tumor nodules: Consequences of a "binding site barrier." *Cancer Res* 51(18):4776–4784.
32. Graff CP, Wittrup KD (2003) Theoretical analysis of antibody targeting of tumor spheroids: Importance of dosage for penetration, and affinity for retention. *Cancer Res* 63(6):1288–1296.
33. Waite CL, Roth CM (2011) Binding and transport of PAMAM-RGD in a tumor spheroid model: The effect of RGD targeting ligand density. *Biotechnol Bioeng* 108(12):2999–3008.
34. Goodman TT, Chen J, Matveev K, Pun SH (2008) Spatio-temporal modeling of nanoparticle delivery to multicellular tumor spheroids. *Biotechnol Bioeng* 101(2):388–399.
35. Lacroix M, Leclercq G (2004) Relevance of breast cancer cell lines as models for breast tumours: An update. *Breast Cancer Res Treat* 83(3):249–289.
36. Cheng J, Khin KT, Davis ME (2004) Antitumor activity of beta-cyclodextrin polymer-camptothecin conjugates. *Mol Pharm* 1(3):183–193.
37. Chaffer CL, Weinberg RA (2011) A perspective on cancer cell metastasis. *Science* 331(6024):1559–1564.
38. Pulaski BA, Ostrand-Rosenberg S (1998) Reduction of established spontaneous mammary carcinoma metastases following immunotherapy with major histocompatibility complex class II and B7.1 cell-based tumor vaccines. *Cancer Res* 58(7):1486–1493.
39. Smith MCP, et al. (2004) CXCR4 regulates growth of both primary and metastatic breast cancer. *Cancer Res* 64(23):8604–8612.